EES Catalysis

Polymer-mediated exsolution and segregation of ruthenium oxides on β-MnO₂ for durable water oxidation in proton-exchange membrane electrolyzers

Yanzhi Zhang,†[ab] Xingyi Zhan,†[ab] Zhihe Wei,†[ab] Chenghao Wang,[ab] Zhangyi Zheng,[ab] Shiwei Mei,[ab] Daqi Song,[ab] Mutian Ma,[ab] Xinyu Zhang,[ab] Xiya Yang,[ab] Tong Zhou,[ab] Jianrong Zeng,[cd] Yang Peng [iD] *[ab] and Zhao Deng [iD] *[ab]

The development of acid-stable and low-noble-metal electrocatalysts for the oxygen evolution reaction (OER) is challenging but demanding for the large-scale application of proton-exchange membrane water electrolyzers (PEMWE). Herein, taking advantage of the densely packed and stable crystalline structure of β-MnO₂ and the dopant-induced lattice strain, a high-performance OER catalyst with low Ru loading is developed *via* the thermally-driven and polymer-mediated exsolution and segregation process. While high-resolution microscopic studies clearly illustrate the Schottky mechanism involved in the formation of polycrystalline RuOₓ-containing grains anchored to the MnO₂ support, spectroscopic findings unveil a significantly altered electronic structure with reduced Mn and Ru chemical states, as well as populated vacancies. Consequently, the best catalyst Ru–MnO₂-PT achieves remarkable OER activity in acidic medium, requiring an overpotential of only 163 mV to reach a current density of 10 mA cm⁻², in addition to excellent electrolytic stability, enabling a prolonged operation of PEMWE for over 2000 hours. This study sheds new light on controllably regulating the exsolution and segregation process of noble metal-doped transition metal oxides for the fabrication of highly robust OER catalysts.

Broader context

Renewable-electricity-driven proton exchange membrane (PEM) water electrolysis for green hydrogen production has the advantages of high current density, high energy efficiency and fast response rates. Currently, the commonly used IrO₂ catalyst for the anode in PEM has bottlenecks such as low element reserves and high price. RuO₂ has relatively high OER activity, but its inherent instability under acidic OER conditions, primarily caused by Ru dissolution, severely limits practical applications. How to effectively suppress Ru dissolution and improve Ru utilization and stability remains a major challenge. In this work, taking advantage of the densely packed and stable crystalline structure of β-MnO₂ and dopant-induced lattice strain, we develop a polymer-mediated exsolution and segregation strategy to controllably expose Ru active sites on β-MnO₂ while mitigating dissolution through strong interfacial coupling. Advanced microscopic and spectroscopic studies unveil the Schottky mechanism for Ru exsolution and segregation, and the modulation of electronic structure through sacrificial pyrolysis of the polymer coating. Compared with traditional IrO₂ and RuO₂ catalysts, the Ru–MnO₂ catalyst developed here has the advantages of high Ru atom utilization and good stability, which can provide an important theoretical and experimental basis for constructing low-precious-metal and long-life PEM water electrolysis devices.

[a] Soochow Institute for Energy and Materials Innovations, Key Laboratory of Advanced Carbon Materials and Wearable Energy Technologies of Jiangsu Province, College of Energy, Soochow University, Suzhou, 215006, P. R. China. E-mail: zdeng@suda.edu.cn, ypeng@suda.edu.cn

[b] Jiangsu Key Laboratory of Advanced Negative Carbon Technologies, Soochow University, Suzhou, 215006, P. R. China

[c] Shanghai Synchrotron Radiation Facility, Shanghai Advanced Research Institute, Chinese Academy of Sciences, 201204, Shanghai, P. R. China

[d] Shanghai Institute of Applied Physics, Chinese Academy of Sciences, 201800, Shanghai, P. R. China

† Yanzhi Zhang, Xingyi Zhan, and Zhihe Wei contributed equally to this work.

Introduction

Renewable-energy-powered water electrolysis has emerged as a cornerstone of the hydrogen economy, offering a sustainable pathway toward carbon neutrality.[1–4] Among the diverse water electrolysis technologies such as alkaline, acidic and solid oxide systems, proton exchange membrane water electrolyzers (PEMWE) distinguish themselves through the merits of high operating current density (>2 A cm⁻²), high voltage efficiency ($>80\%$), rapid response (<100 ms), and inherent adaptability

to unstable energy inputs from solar/wind systems.[5,6] However, in PEMWE the anodic oxygen evolution reaction (OER) under acidic conditions imposes a critical challenge on the stability of electrocatalysts, demanding the use of noble metal oxides.[7–9] Currently, IrO_2 remains the benchmark OER catalyst in PEMWE due to its good catalytic activity and operational durability.[10] Yet, iridium's scarcity (with annual global yield < 8 tons) and exorbitant cost (>US$ 150k per kg) hinder its large-scale application.[11] As an alternative, ruthenium (Ru) has a cost about 1/8th that of Ir, but still contributes significantly to material expenses in PEMWE.[12,13] Moreover, Ru-based catalysts suffer from oxidative dissolution under high OER potentials in acidic media, leading to irreversible performance degradation.[14] To enable cost-effective PEMWE deployment, it is imperative to reduce noble metal usage while enhancing catalyst longevity under harsh operational conditions.

Anchoring noble metal oxides on acid-stable supports is an effective strategy to achieve the goal above. To this end, researchers have devised various tactics, such as doping,[15–17] compositing,[18,19] epitaxial growth,[20,21] and interfacial engineering,[22,23] targeting synergistic activity–stability–cost improvement through multiobjective design. For instance, Ge et al. doped atomistic Ir into γ-MnO_2 and achieved superior activity and stability to commercial IrO_2 by promoting lattice oxygen participation and strengthening Ir–O covalency.[24] In a more recent study, Zhang et al. adopted a ripening-induced embedding strategy to anchor Ir nanoparticles onto cerium oxide by synchronizing the growth rate of the support with the nucleation rate of nanoparticles. This approach enabled long-term PEMWE operation while significantly reducing noble metal usage.[25] Despite these encouraging advances, further efforts are needed to continuously improve the catalyst durability while minimizing noble metal consumption in PEMWE.

Another promising approach to construct heterogeneous catalysts is through elemental exsolution and segregation.[26–28] Given a specific atmosphere, these processes occur when the segregation energy of one metal component in a multinary oxide matrix is lower than that of the others. Leveraging this "inside-out" mechanism, exsolved metal nanoparticles form uniformly on the oxide support, establishing strong interactions with the matrix.[29] This enhances interfacial electron transfer while preventing nanoparticle agglomeration under harsh reaction conditions. Moreover, the composition and morphology of the segregated phase can be finely tuned by adjusting the gas atmosphere and annealing conditions. To date, the majority of oxide supports are limited to perovskites,[30,31] layered double hydroxides (LDHs)[32,33] and spinels,[34,35] offering distinct advantages of high surface area, great thermal stability and superior metal nanoparticle dispersion. These exsolved nanoparticles act as stable active sites during electrocatalysis, with the electronic structure effectively modulated by the underlying support.[36] However, most reported exsolution processes still require high temperature and lack precise control, posing challenges for structure regulation and scalable application.

In this study, we aim to reduce noble metal reliance and extend the longevity of oxygen evolution reaction (OER) catalysts in acidic media by employing MnO_2 as the oxide support to exsolve Ru-based active sites. The selection of β-MnO_2 is

motivated by its densely packed lattice structure, wherein Ru doping could render a metastable state with significant lattice strain, thereby promoting thermally driven exsolution and segregation. Polymer coating is further applied to mediate the exsolution process through sacrificial pyrolysis. Using high-resolution microscopy and spectroscopy, we reveal the formation of polycrystalline RuO_x grains anchored on the MnO_2 support following the Schottky mechanism, concomitant with a significant change of the electronic structure. The optimized catalyst exhibits exceptional OER performance in acidic media, achieving a low overpotential of 163 mV at 10 mA cm^{-2} and outstanding stability, sustaining PEMWE operation for over 2000 hours. This work provides a new strategy for the controlled exsolution and segregation of noble metal-doped transition metal oxides, advancing the design and fabrication of highly durable OER catalysts.

Results and discussion

Theoretical prediction of the exsolution and segregation of Ru from β-MnO_2

By virtue of its 1×1 tunnel structure without support from any alkali/alkaline-earth cations, β-MnO_2 (Pyrolusite) is regarded as one of the most closely packed and thermodynamically stable polymorphs of manganese dioxide. Hence, one would envisage the difficulty to dope such a dense lattice with foreign cations, especially those with a larger radius. To assess the feasibility of Ru doping into β-MnO_2, we began by inspecting the energetics of the constructed Ru–MnO_2 models through density functional theory (DFT) calculations. We first calculated the enthalpy changes for galvanically doping β-MnO_2 with Ru under both stressed and relaxed lattice conditions based on the atomic model shown in Fig. 1a. The results indicate a free energy increase of 0.997 eV for Ru–MnO_2 constrained to the lattice constant of β-MnO_2, in contrast to an exothermic process of -3.22 eV for the fully relaxed structure, of which the unit cell volume increased by 8.97% (Table S1 and Fig. S1). Next, we calculated the internal energy of $Ru_{0.167}Mn_{0.833}O_2$ (with 1/6th of Mn in the lattice replaced by Ru), increasing by 0.35–0.36 eV per unit cell across the temperature range from 0 to 800 K (Fig. 1b and Fig. S2). Apparently, the energy penalty caused by lattice strain far surpasses the enthalpy gain from the galvanic replacement reaction. These results support the feasibility of Ru doping into β-MnO_2 to form meta-stable Ru–MnO_2 under relatively mild conditions.

To investigate the distribution of Ru atoms within the β-MnO_2 lattice, we compared six configurations of $Ru_{0.167}Mn_{0.833}O_2$ with varying Ru dispersity (Fig. S3). The results indicate that, in general, the dispersed Ru arrangements exhibit lower free energies than those of clustered configurations, suggesting that Ru atoms tend to occupy discrete and isolated sites within the β-MnO_2 lattice to form a homogeneous solid solution. We then set to determine the minimal energy required to drive the dispersed bulk Ru atoms to the surface. As shown in Fig. 1c, by reconfiguring the dispersed Ru atoms from their stressed bulk state to surface state, the free energy increased by 0.68 eV due to the offset
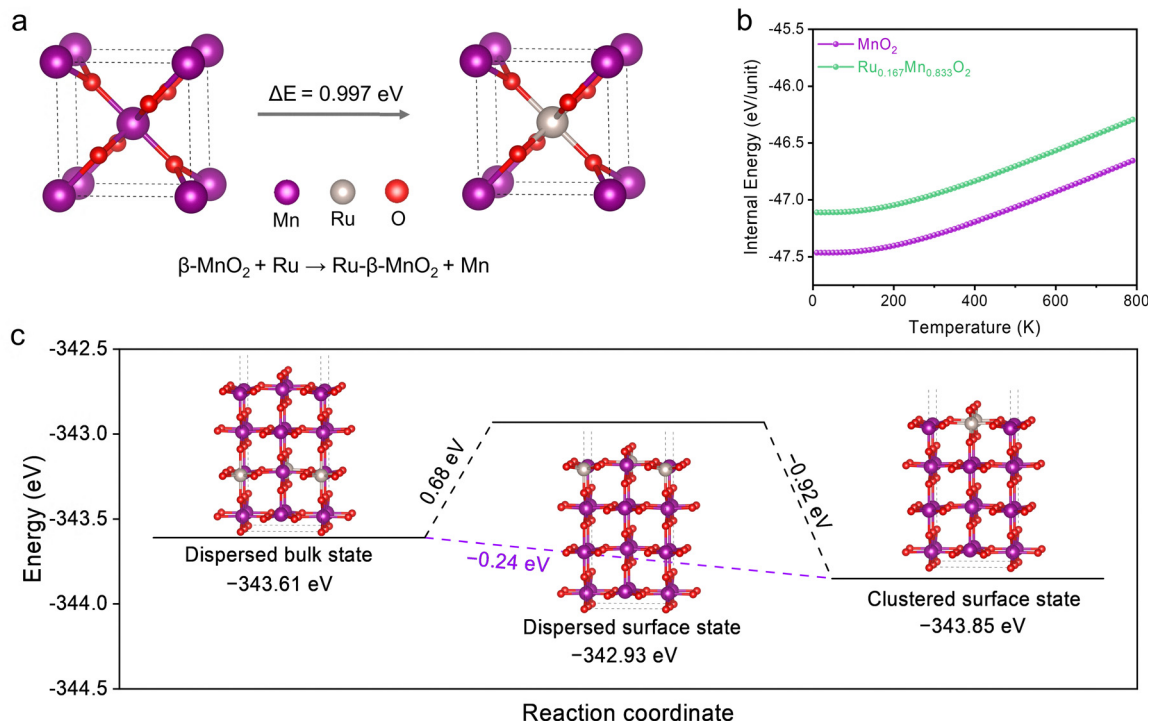
Fig. 1 DFT calculations on the energetics of Ru doping, exsolution and segregation in β-MnO$_2$. (a) Calculated enthalpy for galvanically replacing one Mn atom in β-MnO$_2$ with Ru (models are constrained to the lattice constant). (b) Temperature-dependent internal energy of MnO$_2$ and Ru$_{0.167}$Mn$_{0.833}$O$_2$. (c) Free energy change of Ru–MnO$_2$ transitioning from the dispersed bulk state to the dispersed surface state or clustered surface state.

of lattice strain by the surface energy increase. However, when the surface Ru atoms are grouped together, the free energy of Ru–MnO$_2$ decreased by −0.92 eV, accounting for a total energy drop of −0.24 eV from the initial dispersed bulk state. Thus, the most probable scenario for Ru segregation from β-MnO$_2$ is transiting from the highly dispersed bulk state to the aggregated surface state. Based on the calculation results, we posit that doping Ru into β-MnO$_2$ would result in a meta-stable state of Ru–MnO$_2$, requiring only a marginal energy input, such as modest thermal annealing, to drive Ru exsolution and segregation from the stressed MnO$_2$ lattice. As the atomic radius of Ru (178 pm) is slightly larger than that of Mn (161 pm), the extrusion of Ru atoms would disfavour the formation of Frankel defects but favour the Schottky defects (Fig. S4).[37]

Thermally induced exsolution and segregation of Ru–MnO$_2$

Known for its capability in kinetic control of wet chemistry, microwave-assisted hydrothermal synthesis was employed to synthesize metastable Ru-doped β-MnO$_2$. Compared to the conventional hydrothermal synthesis, the microwave-assisted hydrothermal method typically shortens the reaction time, facilitating industrial scale-up.[38,39] More detailed information about the synthetic procedure is given in the experimental section. Based on the elemental analysis using inductively coupled plasma atomic emission spectroscopy (ICP-AES), the highest Ru doping is limited to ~15% in mass percentage, which is implemented throughout the experimental studies here unless otherwise specified. Utilizing scanning electron microscopy (SEM) and high-resolution transmission electron

microscopy (HR-TEM), we first compared the micro-morphology and lattice structure of the as-synthesized pristine β-MnO$_2$ (denoted as β-MnO$_2$), Ru-doped β-MnO$_2$ (denoted as Ru–MnO$_2$), and thermally treated Ru–MnO$_2$ (denoted as Ru–MnO$_2$-T). β-MnO$_2$ exhibited the typical nanorod structure with a smooth surface (Fig. 2a). TEM images (Fig. 2d and Fig. S5) showed the single-crystalline nature of these nanorods with characteristic (110) facets of 0.311 nm in d-spacing (JCPDS 24-0735). Ru–MnO$_2$ maintained the nanorod morphology of β-MnO$_2$, but with a slightly roughened surface (Fig. 2b). While (110) lattice fringes still dominated the crystals, polycrystalline features were also visualized, especially near the surface (Fig. 2e and Fig. S6). Measurements on the (110) fringes revealed an average d-spacing of 0.313 nm, which is slightly larger than that of pristine β-MnO$_2$. As the atomic radius of Ru is slightly larger than that of Mn, it was reasonable to observe the expanded and stressed lattice in Ru-doped MnO$_2$.

Upon thermal annealing in air at 350 °C for 1 hour, Ru–MnO$_2$-T developed a notably different morphology. Not only the nanorods became more fragmented, but also their surface appeared to be rougher (Fig. 2c). More strikingly, TEM images clearly revealed a newly developed surface layer comprising numerous polycrystalline grains (Fig. 2f and Fig. S7). Most of these grains present only short-range order with discernable lattice fringes, while some are even amorphous. A careful inspection on the lattice constant and orientation revealed that some of the crystalline grains can be assigned to RuO$_2$ (JCPDS 40-1290). Meanwhile, the inner MnO$_2$ (110) lattice spacing measured 0.309 nm (smaller than those of both β-MnO$_2$ and
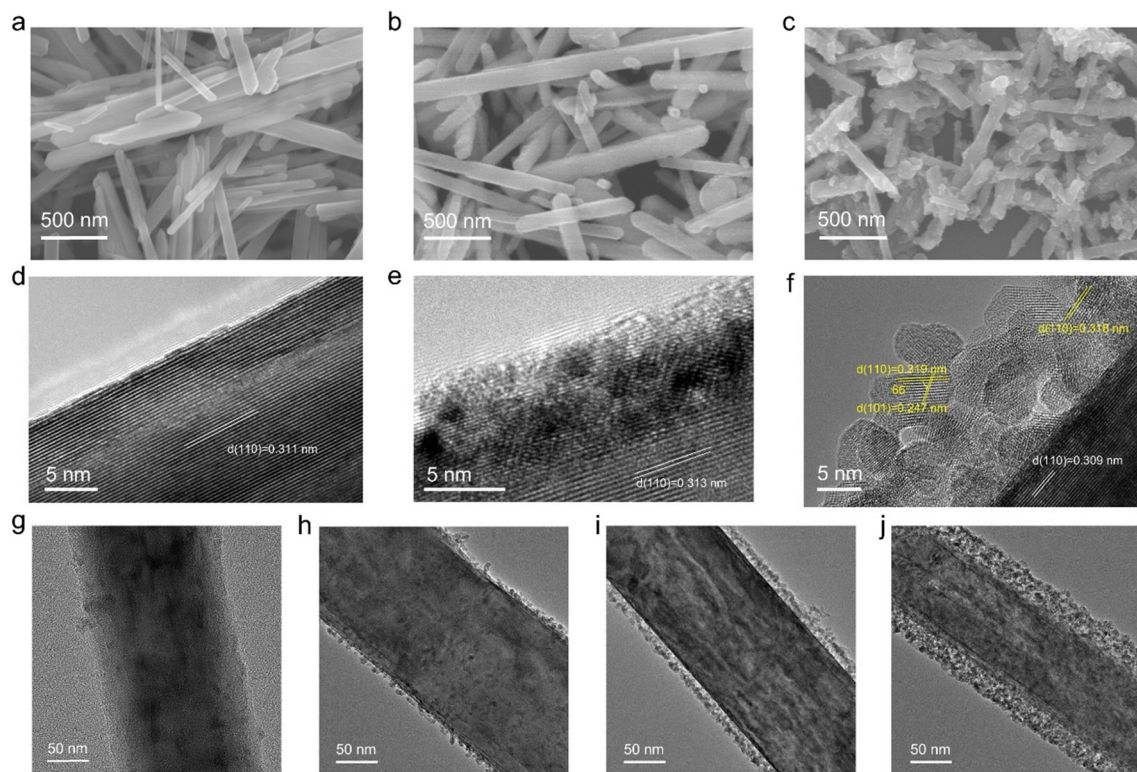
Fig. 2 Microscopic characterization of pristine and Ru-doped β-MnO$_2$ before and after thermal annealing. SEM images of (a) β-MnO$_2$, (b) Ru–MnO$_2$, and (c) Ru–MnO$_2$-T (60 min). TEM images of (d) β-MnO$_2$, (e) Ru–MnO$_2$, and (f) Ru–MnO$_2$-T (60 min). Lattice fringes labelled white correspond to β-MnO$_2$, while those labelled yellow belong to RuO$_2$. TEM images of Ru–MnO$_2$-T upon thermal annealing in air at 350 °C for (g) 0 min, (h) 30 min, (i) 60 min, and (j) 180 min.

Ru–MnO$_2$), indicating contraction of the bulk MnO$_2$ lattice due to the release of lattice strain caused by Ru segregation. Therefore, it is evident that thermal treatment of the meta-stable Ru–MnO$_2$ enables the exsolution of Ru cations, which are then segregated and oxidized on the surface of β-MnO$_2$, forming MnO$_2$/RuO$_2$ heterostructures through the Schottky mechanism.[40]

The Ru exsolution and segregation from Ru–MnO$_2$ was further visualized using *ex situ* TEM images (Fig. 2g–j). After annealing for 30 minutes, numerous small crystals of 5–10 nm size appeared on the surface of β-MnO$_2$ (Fig. 2h and Fig. S8). The number of these crystals continued to grow as the annealing time extended, coalescing to form a core–shell structure after 60 minutes (Fig. 2i and Fig. S7). By the end of the three-hour thermal treatment, the thickness of the surface layer, comprising loosely stacked and coalesced crystalline grains, was up to 30 nm (Fig. 2j and Fig. S9). EDX elemental mapping images further confirmed the enrichment of Ru at the surface of β-MnO$_2$ rods for Ru–MnO$_2$-T as opposed to the homogeneous distribution of Ru in Ru–MnO$_2$ (Fig. S10). These TEM observations enable us to conceive that Ru ions inside the MnO$_2$ lattice, driven by their high oxophilicity and high lattice strain, move towards the surface, leaving vacancies behind. At the surface, the Ru ions are oxidized and aggregated to form RuO$_2$ clusters of varying crystallinity. With time, the vacancies propagate inward, contracting (or even collapsing) the β-MnO$_2$ lattice. This process forms a surface layer comprising a mixture of RuO$_2$ and MnO$_2$ crystals that are loosely attached to the

shrunk β-MnO$_2$ base. Thus, from our comprehensive HR-TEM analysis, it is clear that the exsolution and segregation of Ru from β-MnO$_2$ follow the Schottky mechanism.

Polymer-mediated exsolution and segregation of RuO$_x$ on β-MnO$_2$

Aiming to enhance the cementing of the segregated RuO$_2$ phase and the MnO$_2$ base, we coated the Ru–MnO$_2$ nanorods, prior to thermal treatment, with polyaniline to form an amorphous surface layer (denoted as Ru–MnO$_2$-P; Fig. 3a and Fig. S11). Here, polyaniline was chosen for its suitable decomposition temperature (Fig. S12), matching the annealing temperature of 350 °C used for Ru exsolution. The polyaniline-coated Ru–MnO$_2$ after thermal treatment (Ru–MnO$_2$-PT) also showed a roughened surface, but with a more condensed lattice structure (Fig. 3b–f). Combining HR-TEM, the combustion test (Fig. S13) and Raman analysis (Fig. S14), we were able to conclude the complete pyrolysis of the PANI coating. A close inspection on the lattice fringes revealed that the surface layer is composed of mixed MnO$_2$ and RuO$_2$ features, suggesting the embedding of RuO$_2$ nanodomains within the MnO$_2$ matrix. Similar to previous observations on Ru–MnO$_2$, *ex situ* TEM images provide a dynamic picture of the polymer-mediated Ru exsolution and segregation process. After 30 min of oxidation in air, the amorphous PANI coating initially coated on the Ru–MnO$_2$ surface was significantly reduced (Fig. 3b and c). Segregated RuO$_2$ nanoclusters were clearly seen on the MnO$_2$ surface, with
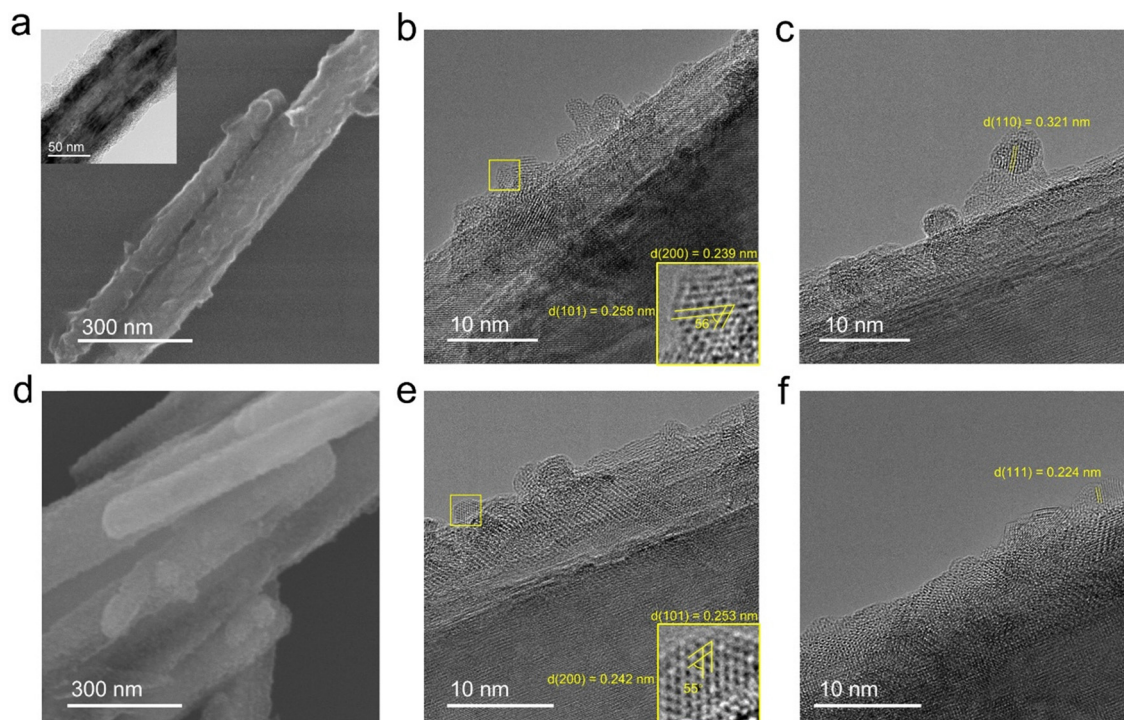
Fig. 3 Microscopic characterization of Ru–MnO₂-P and Ru–MnO₂-PT. (a) SEM and TEM (inset) images of Ru–MnO₂-P. (b) and (c) TEM images of Ru–MnO₂-PT (30 min). (d) SEM image of Ru–MnO₂-PT (180 min). (e) and (f) TEM images of Ru–MnO₂-PT (180 min).

some detached from the β-MnO₂ surface while still embedded within the amorphous coating (Fig. 3c). As the thermal treatment proceeded, the polymer coating was mostly pyrolyzed, leaving a relatively condensed lattice behind. Meanwhile, the previously extruded nanoclusters were detached from the MnO₂ surface along with the pyrolyzed polymer coating. By the end of the three-hour annealing, a rough surface with a mixed lattice structure was observed on Ru–MnO₂-PT, on which small RuO₂

nanoclusters were distinguishable (Fig. 3d–f). Therefore, through sacrificial pyrolysis, the polymer coating helped to anchor the segregated RuO₂ phase to the underlying β-MnO₂ base.

Structural and electronic analyses

The electronic structures of pristine β-MnO₂, Ru–MnO₂-T (180 min, omitted hereafter) and Ru–MnO₂-PT (180 min, omitted hereafter) were analyzed using X-ray photoelectron spectroscopy

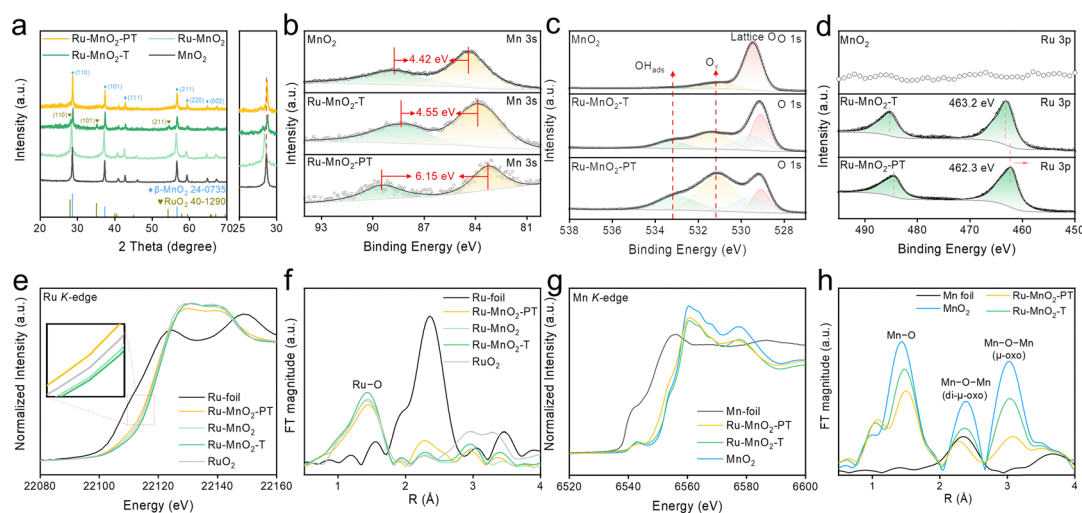Fig. 4 Structural and electronic analyses. (a) XRD patterns of β-MnO₂, Ru–MnO₂, Ru–MnO₂-T, and Ru–MnO₂-PT. The right panel amplifies the shift of the β-MnO₂(110) peaks. XPS (b) Mn 3s, (c) O 1s and (d) Ru 3p spectra of β-MnO₂, Ru–MnO₂-T and Ru–MnO₂-PT. (e) XANES Ru K-edge and (f) the corresponding FT-EXAFS spectra of Ru–MnO₂-T and Ru–MnO₂-PT in reference to RuO₂ and Ru foil. (g) XANES Mn K-edge and (h) the corresponding FT-EXAFS spectra of Ru–MnO₂-T and Ru–MnO₂-PT in reference to MnO₂ and Mn foil.

(XPS) and synchrotron-based X-ray absorption spectroscopy (XAS). Prior to that, XRD patterns were acquired (Fig. 4a). Compared to the pristine β-MnO$_2$, Ru–MnO$_2$ showed a notable shift of the β-MnO$_2$(110) plane toward lower 2θ angles (JCPDS 24-0735),[41,42] corroborating the TEM observation of the expanded lattice. After thermal treatment, the MnO$_2$(110) diffraction peak of Ru–MnO$_2$-T shifted reversibly to higher 2θ angles, which is in line with the contracted lattice observed in TEM images. Additionally, RuO$_2$ peaks (JCPDS 40-1290) of low intensity can be identified, coinciding with the small RuO$_2$ crystallites observed by TEM. As for Ru–MnO$_2$-PT, the 2θ shift of the XRD peaks is negligible when compared to β-MnO$_2$, suggesting the offset of Ru-induced lattice expansion by polymer-mediated Ru segregation. Meanwhile, the peaks of RuO$_2$ are barely visible due to the inhibited surface oxidation upon Ru segregation, which will be detailed later. No carbon-related diffraction peaks were observed, evidencing the complete pyrolysis of the PANI coating, which was further confirmed by the lack of carbonaceous D and G bands in the Raman spectra (Fig. S14).

XPS spectra of Mn 3s splitting (ΔE_{3s}, Fig. 4b), which is caused by electron exchange in the 3s–3d orbitals upon photoelectron ejection and sensitive to the oxidation state of Mn, showed that the Mn valency in Ru–MnO$_2$-T ($\sim$3.9, calculated based on the equation: $AOS_{Mn} = 9.67 - 1.27\Delta E_{3s}$) is close to that of pristine β-MnO$_2$ ($\sim$4.0).[1,43,44] This indicates that the chemical state of Mn in Ru–MnO$_2$-T, despite severe surface reconstruction, is mostly saturated. In stark contrast, the oxidation state of Mn calculated for Ru–MnO$_2$-PT was only $\sim$2.0, suggesting that the pyrolysis of PANI induced a highly reductive Mn state at the surface of the β-MnO$_2$ nanorods. Correspondingly, XPS O 1s spectra revealed a significantly intensified peak at 531.19 eV for vacancy-related oxygen species (O$_v$), which indicates an oxygen-deficient lattice structure at the surface of Ru–MnO$_2$-PT (Fig. 4c). While XPS Ru 3p spectra revealed no signal for pristine β-MnO$_2$ as expected, both Ru–MnO$_2$-T and Ru–MnO$_2$-PT samples displayed a strong Ru 3p doublet (Fig. 4d). The binding energies of the Ru peaks for Ru–MnO$_2$-T are higher than those for Ru–MnO$_2$-PT by $\sim$0.96 eV, in resonance with the high Mn valency of the former. Therefore, we can conclude that pyrolysis of the PANI coating significantly altered the surface electronic structure of the composite with reduced chemical states of both Ru and Mn.

The above argument was further validated by systematic XAS studies on β-MnO$_2$, Ru–MnO$_2$, Ru–MnO$_2$-T and Ru–MnO$_2$-PT. X-ray absorption near edge structure (XANES) spectra of the Ru K-edge showed the photon energy of edge absorption follows the order: Ru–MnO$_2$-PT < RuO$_2$ < Ru–MnO$_2$ < Ru–MnO$_2$-T (Fig. 4e), reflecting the XPS results above. Due to the synthesis involving KMnO$_4$ and the ultrafine RuO$_2$ crystallites of strong oxophilicity, it was reasonable to observe that both Ru–MnO$_2$ and Ru–MnO$_2$-T exhibit even higher formal oxidation numbers than commercial RuO$_2$. In the Fourier-transform extended X-ray absorption fine structure in the R space, all samples exhibited a prominent peak at $\sim$1.43 Å (Fig. 4f), which is ascribed to the Ru–O bonding in the first coordination sphere. Consistent with the valency trend, the Ru–O coordination

number also follows the order: Ru–MnO$_2$-PT (5.84 $\pm$ 0.66) < RuO$_2$ (6.00 $\pm$ 1.43) < Ru–MnO$_2$ (6.31 $\pm$ 0.86) < Ru–MnO$_2$-T (6.52 $\pm$ 0.9) (Fig. S15 and Table S2), evidencing that the Ru species in Ru–MnO$_2$-T are highly oxidized, whereas those in Ru–MnO$_2$-PT are undercoordinated. Moreover, a small Ru–Ru signal can be discerned at R = 2.28 Å for Ru–MnO$_2$-PT, suggesting that a small portion of the segregated Ru species might even take the metallic form. This rationalizes the low average valency of Ru in Ru–MnO$_2$-PT as observed by both XPS and XANES. Based on these spectral findings, we realized that it would be more accurate to refer to the segregated Ru phase on the surface of Ru–MnO$_2$-PT as RuO$_x$, instead of RuO$_2$. XANES spectra of the Mn K-edge showed the oxidation state of Mn follows the order: Ru–MnO$_2$-PT < Ru–MnO$_2$-T < MnO$_2$ (Fig. 4g), coincident with the XPS Mn 3s results. FT-EXAFS spectra in the R space revealed a significantly reduced Mn–O coordination number and suppressed μ-oxo moieties, corroborating the more reductive and chaotic β-MnO$_2$ lattice induced by PANI pyrolysis.

Based on the comprehensive microscopic and spectroscopic characterizations above, we now stand on firm ground to draw an explicit picture of the microstructure and electronic states of Ru–MnO$_2$-T and Ru–MnO$_2$-PT: (1) without PANI coating, segregation of Ru from β-MnO$_2$ following the Schottky mechanism causes a devastating morphological change while impacting less on the chemical states of Mn and Ru; (2) with PANI coating, Ru segregation concurrent with PANI pyrolysis results in a more coherent surface crystallinity, but at the cost of drastically altered chemical states and electronic structure. Keeping these structural and electronic attributes in mind, we proceed to compare their OER characteristics in acidic medium.

OER characteristics in the three-electrode electrolytic cell

We began by studying the amount of Ru doping on the OER performance of Ru–MnO$_2$-T. By ramping up the concentration of the RuCl$_3$ precursor in the microwave reaction, we were able to incrementally increase the Ru content in β-MnO$_2$ from 2.8% to 14.3% (Table S3). Adding more RuCl$_3$·3H$_2$O did not increase the Ru content without altering the morphology and crystallinity of β-MnO$_2$, as evidenced by the broadened and diminished XRD pattern of Ru$_{14.3\%}$–MnO$_2$-T (Fig. S16). Thus, as mentioned above, we constrained our highest doping quantity not to surpass 15% and abbreviate Ru$_{14.3\%}$–MnO$_2$-T as Ru–MnO$_2$-T. Linear sweep voltammetry (LSV) curves recorded in 0.5 M H$_2$SO$_4$ showed that the OER current density at a given potential increased with the increasing Ru doping as expected (Fig. S17), confirming that Ru is indeed responsible for the OER activity.

We then compared the samples of Ru–MnO$_2$-T and Ru–MnO$_2$-PT against the commercial RuO$_2$ benchmark and the β-MnO$_2$ control. Impressively, Ru–MnO$_2$-PT exhibited a low overpotential of 163 mV to reach a current density of 10 mA cm^{-2} (η_{10}), which is much superior to that of Ru–MnO$_2$-T (178 mV), RuO$_2$ (335 mV) and β-MnO$_2$ (729 mV) (Fig. 5a). To investigate the intrinsic activity of the catalysts by excluding the convolution from specific surface area, electrochemical active surface area (ECSA) was estimated by measuring the double layer
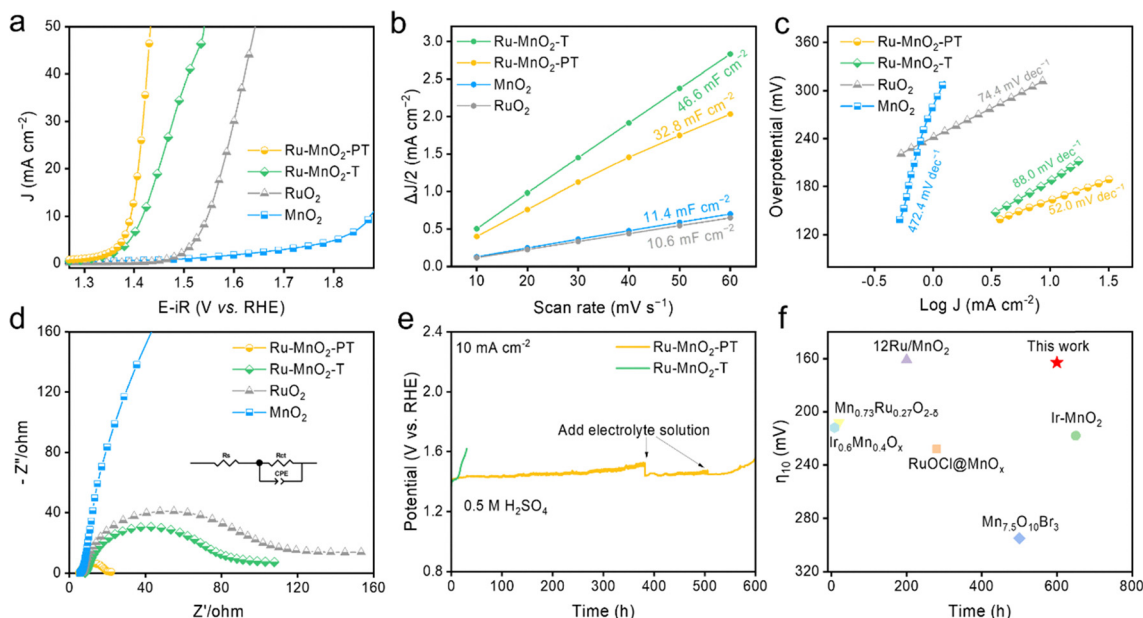
Fig. 5 OER performance metrics of Ru–MnO$_2$-T and Ru–MnO$_2$-PT in 0.5 M H$_2$SO$_4$ in reference to RuO$_2$ and β-MnO$_2$. (a) LSV curves at a scan rate of 10 mV s^{-1}. (b) Measurements of double layer capacitance (C_{dl}) to estimate ECSA. (c) Tafel slopes. (d) EIS spectra recorded at 1.45 V. (e) Chronopotentiometric V–t curves at 10 mA cm^{-2}. (f) Comparison of η_{10} and operational stability in the three-electrode cell.

capacitance (C_{dl}) (Fig. 5b and Fig. S18 and Table S4), which is conceivable considering the highly roughened surface Ru–MnO$_2$-T and Ru–MnO$_2$-PT due to Ru exsolution and segregation. After normalizing the LSV curves to ECSA, both Ru–MnO$_2$-T and Ru–MnO$_2$-PT still exhibited a much higher activity than that of RuO$_2$ (Fig. S19), highlighting their superior intrinsic activity and noble metal utilization.

Measurement of the LSV curves near the onset potential revealed a Tafel slope of 52.0 mV dec^{-1} for Ru–MnO$_2$-PT, followed by RuO$_2$ (74.4 mV dec^{-1}), Ru–MnO$_2$-T (88.0 mV dec^{-1}) and β-MnO$_2$ (472.4 mV dec^{-1}), corroborating the fast electrokinetics of Ru–MnO$_2$-PT after minimizing the interference from concentration polarization (Fig. 5c). Electrochemical impedance spectra acquired at 1.45 V under OER conditions revealed a remarkably small charge transfer resistance (R_{ct}) of only 13.2 Ω for Ru–MnO$_2$-PT, in contrast to those of Ru–MnO$_2$-T (65 Ω), RuO$_2$ (144.9 Ω) and β-MnO$_2$ (1485 Ω) (Fig. 5d). This phenomenon can be partially attributed to the high OV content with improved electrical conductivity (Fig. S20), and more importantly, the highly active RuO$_x$ sites of Ru–MnO$_2$-PT that greatly expedited the electron transport and transfer kinetics. More remarkably, in the three-electrode cell Ru–MnO$_2$-PT demonstrated a stable operation at 10 mA cm^{-2} for over 600 hours, during which the test was even affected by electrolyte evaporation (Fig. 5e). By contrast, despite the low initial η_{10} (178 mV), Ru–MnO$_2$-T only lasted for 30 hours before the cathodic potential increased to 1.6 V (Fig. S21). We surmise that the loosely stacked RuO$_2$ nanocrystals segregated from Ru–MnO$_2$-T might account for its short operational lifetime. Above all, the low η_{10} value of 163 mV, in conjunction with the prolonged operation over 600 hours, ranks Ru–MnO$_2$-PT as one

of the most advanced MnO$_x$-based OER catalysts reported so far (Fig. 5f and Table S5).

OER performance in PEMWE

To further validate the practical application of Ru–MnO$_2$-PT in PEMWE for hydrogen production, both the cathode catalyst (20% Pt/C) and the anode catalyst (Ru–MnO$_2$-PT) were coated onto the Nafion-115 membrane for constructing a membrane electrode assembly operating at 80 °C (Fig. 6a and Fig. S22 and Table S6). In our study, the anode catalyst loading was optimized at 1.5 mg$_{Ru}$ cm^{-2} to assure a stable MEA operation while minimizing the Ru usage. Once the Ru loading was reduced from 1.5 to 0.75 mg$_{Ru}$ cm^{-2}, the MEA cell voltage increased from 1.48 to 1.78 V during the 800-h stability test at 100 mA cm^{-2} (Fig. S23). Under the galvanostatic mode, ramping the current density stepwise from 100 to 1000 mA cm^{-2} led to an increase in cell voltage from 1.40 to 1.82 V, attesting to the high activity of the catalysts (Fig. 6b and Fig. S24). Keeping the operating current density at 100 mA cm^{-2}, the PEMWE was able to operate steadily for over 2000 hours with a voltage degradation rate of only 0.167 mV h^{-1} (Fig. 6c). Further increasing the galvanostatic current density to 500 mA cm^{-2}, the cell was still able to sustain a prolonged operation for over 300 hours, exceeding the commercial RuO$_2$ benchmark and most reported acidic OER catalysts of low noble metal loading (Fig. 6d and Table S5). After the prolonged stability test, SEM and TEM images revealed partial dissolution of MnO$_2$ rods (Fig. S25). Post-mortem XPS analysis showed a reduction in the Mn 3s splitting from 6.55 to 6.34 eV, while the Ru 3p peak shifted from 462.3 to 463.0 eV (Fig. S26). These changes indicate an increase in the valence states of both Mn and Ru. Consequently, the failure mechanism is attributed
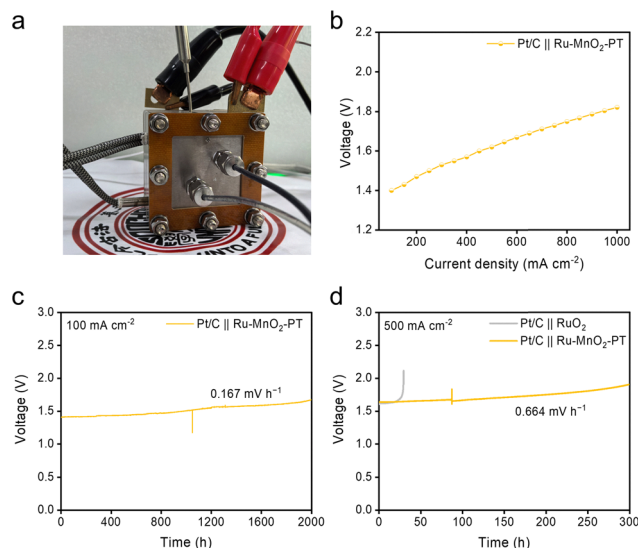
Fig. 6 Performance of Ru–MnO$_2$-PT in PEMWE. (a) Photograph of the PEMWE device. (b) V–I plot. (c) Chronopotentiometric V–t curve at 100 mA cm^{-2}. (d) Chronopotentiometric V–t curve at 500 mA cm^{-2} acquired on PEMWE utilizing Pt/C and RuO$_2$ or Ru–MnO$_2$-PT as the cathode and anode catalysts, respectively.

to Ru and Mn oxidation to higher valence states, leading to their partial dissolution.[45] Further increasing the galvanostatic current density to 1 A cm^{-2}, Ru–MnO$_2$-PT was able to sustain a stable PEMWE operation (4 cm^2 active area) for over 100 h at a low voltage degradation rate of 0.7 mV h^{-1}. Without any iR/HFR correction, the cell voltage increased from 1.80 to 1.87 V at 80 °C under 50 mL min^{-1} water feed, promising for industrial operations (Fig. S27).

Conclusions

In summary, we have successfully developed a high-performance OER catalyst based on MnO$_2$ with low Ru loading through the thermally driven exsolution and segregation process. Utilizing high-resolution TEM images, we show explicitly the temporal thickening of the segregation layer, comprising a large number of polycrystalline grains formed through the Schottky mechanism. To enhance the cementing of the segregated RuO$_x$ nanocrystals, polyaniline was applied as the sacrificial coating and structural modulator during annealing. The polymer-mediated segregation process resulted in a more condensed surface lattice but a significantly altered electronic structure, dramatically reducing the chemical states of Mn and Ru while populating the vacancy-related oxygens. As a result, the best catalyst Ru–MnO$_2$-PT achieved remarkable OER activity in acidic medium, requiring an overpotential of only 163 mV to reach a current density of 10 mA cm^{-2}. Moreover, Ru–MnO$_2$-PT demonstrated excellent electrocatalytic stability, enabling a prolonged operation of PEMWE for over 2000 hours, exceeding most reported acidic OER catalysts. By controllably regulating the segregation process of noble metal-doped transition metal oxides, this study offers a novel strategy for the design and fabrication of high-performance OER catalysts

with extended durability and alleviated noble metal dependency, paving the way for large-scale deployment of PEMWE systems at reduced cost.

Author contributions

Y. Z., Y. P. and Z. D. conceived and designed the studies. Y. Z. and Z. W. synthesized the materials, investigated their electrochemical properties, analyzed the data and wrote the paper. X. Z. performed the DFT calculations and result analyses. C. W. and X. Z. contributed to the materials synthesis and electrochemical measurements. Y. Z., Z. Z. and M. M. performed the PEM electrolyzer tests, SEM tests, and Raman test. S. M. and D. S. supported the TEM characterization and analysis. X. Y. and T. Z. provided ICP and XRD support. J. Z. supported beamline BL13SSW at Shanghai Synchrotron Radiation Facility for the XAFS measurements. Z. W., Y. P., and Z. D. acquired the financial support for the project. All authors discussed the results and critically reviewed the manuscript.

Conflicts of interest

There are no conflicts to declare.

Data availability

All relevant data are included in the main text and its SI. Supplementary information: Experimental section and supplementary figures and tables. See DOI: https://doi.org/10.1039/d5ey00227c.

Acknowledgements

Notes and references

1 A. Li, S. Kong, K. Adachi, H. Ooka, K. Fushimi, Q. Jiang, H. Ofuchi, S. Hamamoto, M. Oura, K. Higashi, T. Kaneko, T. Uruga, N. Kawamura, D. Hashizume and R. Nakamura, *Science*, 2024, **384**, 666–670.
2 J. Huang, C. N. Borca, T. Huthwelker, N. S. Yüzbasi, D. Baster, M. El Kazzi, C. W. Schneider, T. J. Schmidt and E. Fabbri, *Nat. Commun.*, 2024, **15**, 3067.

3 T. Liu, C. Chen, Z. Pu, Q. Huang, X. Zhang, A. M. Al-Enizi, A. Nafady, S. Huang, D. Chen and S. Mu, *Small*, 2024, **20**, 2405399.

4 J. Cao, D. Zhang, B. Ren, P. Song and W. Xu, *Energy Environ. Sci.*, 2024, **17**, 5911–5921.

5 K. Zhang, X. Liang, L. Wang, K. Sun, Y. Wang, Z. Xie, Q. Wu, X. Bai, M. S. Hamdy, H. Chen and X. Zou, *Nano Res. Energy*, 2022, **1**, 9120032.

6 R. A. Abdelsalam, M. Mohamed, H. E. Z. Farag and E. F. El-Saadany, *Energy Convers. Manage.*, 2024, **319**, 118907.

7 J. Xu, Y. Yang, H. Jin, Y. Zheng and S.-Z. Qiao, *Chem*, 2025, **11**, 102305.

8 R. Qin, G. Chen, X. Feng, J. Weng and Y. Han, *Adv. Sci.*, 2024, **11**, 2309364.

9 X. Wei, S. Sharma, A. Waeber, D. Wen, S. N. Sampathkumar, M. Margni, F. Maréchal and J. Van Herle, *Joule*, 2024, **8**, 3347–3372.

10 X. Xiong, J. Tang, Y. Ji, W. Xue, H. Wang, C. Liu, H. Zeng, Y. Dai, H.-J. Peng, T. Zheng, C. Xia, X. Liu and Q. Jiang, *Adv. Energy Mater.*, 2024, **14**, 2304479.

11 S. Ge, R. Xie, B. Huang, Z. Zhang, H. Liu, X. Kang, S. Hu, S. Li, Y. Luo, Q. Yu, J. Wang, G. Chai, L. Guan, H.-M. Cheng and B. Liu, *Energy Environ. Sci.*, 2023, **16**, 3734–3742.

12 C. Lin, J.-L. Li, X. Li, S. Yang, W. Luo, Y. Zhang, S.-H. Kim, D.-H. Kim, S. S. Shinde, Y.-F. Li, Z.-P. Liu, Z. Jiang and J.-H. Lee, *Nat. Catal.*, 2021, **4**, 1012–1023.

13 https://matthey.com/products-and-markets/pgms-and-circularity/pgm-management/.

14 L. Deng, S.-F. Hung, Z.-Y. Lin, Y. Zhang, C. Zhang, Y. Hao, S. Liu, C.-H. Kuo, H.-Y. Chen, J. Peng, J. Wang and S. Peng, *Adv. Mater.*, 2023, **35**, 2305939.

15 X. Ping, Y. Liu, L. Zheng, Y. Song, L. Guo, S. Chen and Z. Wei, *Nat. Commun.*, 2024, **15**, 2501.

16 Q.-Q. Yan, D.-X. Wu, S.-Q. Chu, Z.-Q. Chen, Y. Lin, M.-X. Chen, J. Zhang, X.-J. Wu and H.-W. Liang, *Nat. Commun.*, 2019, **10**, 4977.

17 J. Xu, C.-C. Kao, H. Shen, H. Liu, Y. Zheng and S.-Z. Qiao, *Angew. Chem., Int. Ed.*, 2024, **64**, e202420615.

18 X.-Y. Zhang, H. Yin, C.-C. Dang, H. Nie, Z.-X. Huang, S.-H. Zheng, M. Du, Z.-Y. Gu, J.-M. Cao and X.-L. Wu, *Angew. Chem., Int. Ed.*, 2025, **64**, e202425569.

19 Y. Gao, X. Sun, G. A. M. Mersal, A. Alhadhrami, M. M. Ibrahim, Y. Hou, W. Liu, D. Bildan, H. Algadi and T. X. Liu, *Adv. Compos. Hybrid Mater.*, 2025, **8**, 117.

20 Z. Fan, Z. Luo, X. Huang, B. Li, Y. Chen, J. Wang, Y. Hu and H. Zhang, *J. Am. Chem. Soc.*, 2016, **138**, 1414–1419.

21 Y. Zhang, Z. Li, H. Jang, M. G. Kim, J. Cho, S. Liu, X. Liu and Q. Qin, *Adv. Mater.*, 2025, **37**, 2501586.

22 Z. Yang, Y. Ding, W. Chen, S. Luo, D. Cao, X. Long, L. Xie, X. Zhou, X. Cai, K. Liu, X.-Z. Fu and J.-L. Luo, *Adv. Mater.*, 2025, **37**, 2417777.

23 Y. Cheng, H. Wang, T. Qian and C. Yan, *EnergyChem*, 2022, **4**, 100074.

24 Z. Shi, Y. Wang, J. Li, X. Wang, Y. Wang, Y. Li, W. Xu, Z. Jiang, C. Liu, W. Xing and J. Ge, *Joule*, 2021, **5**, 2164–2176.

25 W. Shi, T. Shen, C. Xing, K. Sun, Q. Yan, W. Niu, X. Yang, J. Li, C. Wei, R. Wang, S. Fu, Y. Yang, L. Xue, J. Chen, S. Cui, X. Hu, K. Xie, X. Xu, S. Duan, Y. Xu and B. Zhang, *Science*, 2025, **387**, 791–796.

26 L. Zhao, Z. Tao, M. You, H. Xiao, S. Wang, W. Ma, Y. Huang, B. He and Q. Chen, *Adv. Sci.*, 2024, **11**, 2309750.

27 J. Oh, S. Joo, C. Lim, H. J. Kim, F. Ciucci, J.-Q. Wang, J. W. Han and G. Kim, *Angew. Chem., Int. Ed.*, 2022, **61**, e202204990.

28 Y. Chen, M. S. Duyar, R. Han, F. He, X. Sun, Y. Chen, W. Liu and J. Liu, *Mater. Today*, 2024, **75**, 259–284.

29 D. Neagu, G. Tsekouras, D. N. Miller, H. Ménard and J. T. S. Irvine, *Nat. Chem.*, 2013, **5**, 916–923.

30 S. Kim, J. Lee, Y. B. Kim, D. Oh, J. K. Kim, B. Koo, H. Kim, G. H. Jung, M. Kim, G. Doo, J. Seo, T. J. Lim, K. Kim, J. W. Han and W. Jung, *ACS Nano*, 2025, **19**, 10026–10037.

31 H. Kim, C. Lim, J. Gu, H. Y. Jeong, J. W. Han, J.-H. Jang and Y. Bu, *Adv. Energy Mater.*, 2024, **14**, 2401307.

32 L. Lv, Z. Yang, K. Chen, C. Wang and Y. Xiong, *Adv. Energy Mater.*, 2019, **9**, 1803358.

33 Z. Li, J. Liu, R. Shi, G. I. N. Waterhouse, X.-D. Wen and T. Zhang, *Adv. Energy Mater.*, 2021, **11**, 2002783.

34 X. Zou, Q. Lu, J. Wu, K. Zhang, M. Tang, B. Wu, S. She, X. Zhang, Z. Shao and L. An, *Adv. Funct. Mater.*, 2024, **34**, 2401134.

35 E. A. Smal, M. N. Simonov, N. V. Mezentseva, T. A. Krieger, T. V. Larina, A. A. Saraev, T. S. Glazneva, A. V. Ishchenko, V. A. Rogov, N. F. Eremeev, E. M. Sadovskaya and V. A. Sadykov, *Appl. Catal., B*, 2021, **283**, 119656.

36 Y. Luo, D. Zhang, T. Liu, X. Chang, J. Wang, Y. Wang, X.-K. Gu and M. Ding, *Adv. Funct. Mater.*, 2024, **34**, 2403922.

37 S. Moxon, J. Skelton, J. S. Tse, J. Flitcroft, A. Togo, D. J. Cooke, E. Lora da Silva, R. M. Harker, M. T. Storr, S. C. Parker and M. Molinari, *J. Mater. Chem. A*, 2022, **10**, 1861–1875.

38 L.-Y. Meng, B. Wang, M.-G. Ma and K.-L. Lin, *Mater. Today Chem.*, 2016, **1**, 63–83.

39 R. Nagahata and K. Takeuchi, *Chem. Rec.*, 2019, **19**, 51–64.

40 W. Schottky, *Z. Phys. Chem., Abt. B*, 1935, **29**, 335.

41 Y. Qin, Y. Liu, Y. Zhang, Y. Gu, Y. Lian, Y. Su, J. Hu, X. Zhao, Y. Peng, K. Feng, J. Zhong, M. H. Rummeli and Z. Deng, *ACS Catal.*, 2023, **13**, 256–266.

42 H. Li, H. Yao, X. Sun, C. Sheng, W. Zhao, J. Wu, S. Chu, Z. Liu, S. Guo and H. Zhou, *Chem. Eng. J.*, 2022, **446**, 137205.

43 E. S. Ilton, J. E. Post, P. J. Heaney, F. T. Ling and S. N. Kerisit, *Appl. Surf. Sci.*, 2016, **366**, 475–485.

44 M. C. Biesinger, B. P. Payne, A. P. Grosvenor, L. W. M. Lau, A. R. Gerson and R. S. C. Smart, *Appl. Surf. Sci.*, 2011, **257**, 2717–2730.

45 L. Wang, Q. Pan, X. Liang and X. Zou, *ChemSusChem*, 2025, **18**, e202401220.